A Computational Study of Bluntness Vortex Shedding Noise Generated by a Small Canonical Rotor for UAM Applications

Joshua D. Blake
Research Aerospace Engineer

Christopher S. Thurman
Research Aerospace Engineer

Nikolas S. Zawodny
Senior Research Engineer

Aeroacoustics Branch
NASA Langley Research Center
Hampton, VA, USA

ABSTRACT

A hybrid RANS/LES simulation of the Ideally Twisted Rotor (ITR) in hover was interrogated to identify bluntness vortex shedding (BVS) and determine the contribution to the predicted rotor broadband self-noise. Three rotor blade stations were extracted to study spanwise variations in the BVS shedding frequency and amplitude. Corresponding 2-D airfoil simulations were performed to evaluate a simplified modeling approach that effectively isolates BVS. The BVS shedding frequencies predicted by the 2-D airfoil simulations differed by less than 2% from the corresponding rotor stations in the 3-D simulation. The increased computational cost incurred by performing 3-D airfoil simulations did not lead to a worthwhile increase in simulation fidelity. Farfield noise was predicted for the three rotor stations and the 2-D airfoil simulations, and trends in frequency agreed well. The 2-D approach overpredicted the 3-D peak amplitudes by 5–10 dB. This work demonstrates that 2-D hybrid RANS/LES airfoil simulations can be used to investigate BVS noise trends on the ITR.

INTRODUCTION

The emerging and rapidly developing AAM (Advanced Air Mobility) industry and the UAM (Urban Air Mobility) subcategory in particular have brought rotor acoustics to the forefront in the past decade. UAM vehicles will see frequent operation in environments with dense population centers, and vehicle noise is likely to be a significant factor to community acceptance. Propeller or rotor noise is one of the main contributors to AAM and UAM vehicle noise (Ref. 1) and has already become a driving factor in vehicle design. The majority of these vehicles feature electrically driven propulsion and multiple rotors or propellers. This dependency on rotor-based propulsion highlights the critical need for fundamental investigations into the noise of rotors operating in UAM-relevant conditions.

Subscale experiments can provide performance characteristics and acoustic information on the tonal (i.e., deterministic) and broadband (i.e., nondeterministic) noise sources generated by UAM rotors. The dominant tonal noise sources that occur at the fundamental blade passage frequency (BPF) can often be predicted with low-fidelity or computational approaches. However, separating out experimental rotor broadband noise into its component sources is difficult without advanced flow visualization or instrumentation techniques. Low-fidelity analytical or semiempirical models can show trends in component noise sources (Refs. 2, 3), but often fall short when used outside their intended application range, as is often the case for AAM/UAM vehicles (Ref. 4). Computational fluid dynamics (CFD) can reveal high-fidelity details of noise-generating phenomena (Refs. 5, 6), but often at a high computational cost. Ultimately, a combination of several approaches is needed to understand the complex aerodynamic and acoustic environment of a rotor and to identify individual rotor broadband noise sources.

Bluntness vortex shedding (BVS) is a known self-noise source (Refs. 7, 8) caused by an alternating vortex shedding (see Figure 1) that occurs in the near-wake of airfoils with a thick or blunt trailing edge (Refs. 7, 9). This shedding results in distinct tones due to regions of alternating high and low incident pressure at the trailing edge (Refs. 7, 9). Vortices are highly coherent in the spanwise direction (Refs. 10–12), and, therefore, BVS can be considered a quasi-2-D flow phenomenon (Ref. 9). Since the dominant BVS frequency is thought to scale with airfoil geometry (i.e., trailing edge thickness and chord) and flow speed (Refs. 7, 8), BVS is considered tonal in the stationary reference frame of a 2-D airfoil section. However, given that the local flow conditions along a rotor blade vary at each radial and azimuthal station, BVS gener-

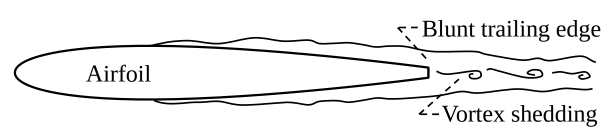

Figure 1. BVS noise source diagram adapted from Brooks, Pope, and Marcolini (Ref. 8).

Presented at the Vertical Flight Society's 81st Annual Forum & Technology Display, Virginia Beach, VA, USA, May 20–22, 2025.

ated at spanwise sections of a rotor blade is considered a form of nondeterministic, self-generated broadband noise in a rotating system.

CFD has been used to simulate airfoil BVS with a variety of turbulence modeling approaches including unsteady RANS (Reynolds-averaged Navier-Stokes), LES (Large Eddy Simulations), and DNS (Direct Numerical Simulation). Wind turbine blade sections with blunt trailing edges have been investigated with unsteady RANS (Ref. 12) and hybrid RANS/LES (Ref. 13) approaches. Using 2-D unsteady RANS, strong vortex shedding was observed from the blunt trailing edge of a slat in a high-lift airfoil (Ref. 14). BVS has been observed in 2-D DNS (Ref. 9) and 3-D LES simulations (Refs. 15, 16) of more canonical airfoils with blunt trailing edges. A more recent study focused on the reduction of BVS through serrated leading edges using IDDES (Improved Delayed Detached Eddy Simulation) (Ref. 17).

A hybrid RANS/LES approach effectively isolates BVS from other self-noise sources (Ref. 8) such as turbulent boundary layer trailing edge noise (TBL-TE) and laminar boundary layer vortex shedding noise (LBL-VS). For an airfoil at a low angle of attack, a hybrid RANS/LES simulation approach ideally maintains RANS mode in the boundary layer and then switches to LES mode just downstream of a blunt trailing edge. Using RANS in the boundary layer eliminates resolved boundary layer turbulence and laminar separation bubbles, which eliminates TBL-TE and LBL-VS noise, respectively. Using LES mode in the near-wake allows vortex shedding to develop, leading to BVS noise. Table 1 shows that BVS is the main self-noise mechanism that would be predicted by a hybrid RANS/LES airfoil simulation.

Table 1. Predicted self-noise sources.

Turbulence Model	TBL-TE	LBL-VS	BVS
RANS	no	no	no
Hybrid RANS/LES	no	no	yes
LES	yes	yes	yes

Low-fidelity predictions (Ref. 3) of a subscale, Ideally Twisted Rotor (ITR) in hover suggested that BVS was a significant contributor to the rotor broadband spectra at frequencies higher than 10 kHz. Additionally, BVS was observed in CFD simulations of the ITR through visualizations of the near-wake at the 75% blade span location (Ref. 6). Several distinct frequency peaks were identified in the simulated broadband rotor spectra that could correspond to BVS shedding. The ITR has a thick trailing edge relative to the chord (1.54%), which increases the possibility of strong BVS in the broadband spectra. These results indicate that BVS generated by the ITR should be investigated in greater depth.

In this paper, the authors revisit the baseline condition of the ITR to investigate BVS and its contribution to the simulated broadband rotor noise. The main research objective is to determine whether a 2-D hybrid RANS/LES airfoil simulation approach can be used to predict BVS on a rotor and if there are significant differences in the dominant vortex shedding frequency predicted by 2-D airfoil, 3-D airfoil, and rotor simulations. The underlying research question is whether 3-D flow effects are significant enough to invalidate predictions made using a model that assumes an infinitely coherent 2-D vortex.

The outline of the paper is as follows: the ITR geometry is discussed, along with the simulation setup parameters. Then the results section first investigates the flowfield from the previous rotor simulation (Refs. 6, 18) to identify BVS. Then, selected blade stations are extracted along the rotor where BVS is observed to be a dominant feature, and 2-D and 3-D airfoil simulations are performed at the same representative flow conditions. Fluctuating wall pressures from the rotor and airfoil simulations are used to predict farfield BVS noise. A final 2-D simulation is performed to determine the effects of calculating the effective angle of attack from BEMT (blade element momentum theory) instead of a 3-D rotor simulation. Finally, conclusions are given on the effectiveness of this simulation approach.

ROTOR GEOMETRY AND METHODOLOGY

The ITR (shown in Figure 2) is a subscale canonical rotor that was designed to induce a uniform inflow and minimize induced power in hover. The four-bladed rotor's radius is R = 0.15875 m (6.25 in.). The chord, c, is a constant 0.03175 m (1.25 in.) along the blade span. The design operating condition is 5500 RPM in hover, which corresponds to a tip Mach number of 0.269 at sea-level standard day conditions. The ITR was defined with an NACA 0012 airfoil, but the trailing edge was thickened about the camber line by flaring and smoothly rounding the airfoil using OpenVSP (Ref. 19). Additional details of the ITR's design and the accompanying experiments can be found in Pettingill et al. (Ref. 3).

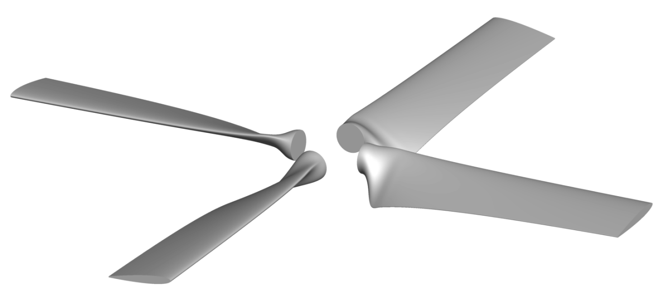

Figure 2. Geometry of the ITR.

OVERFLOW2 (Ref. 20), a structured Navier-Stokes solver with overset grid capabilities (Ref. 21), was used for the rotor and airfoil simulations. A dual-time approach was used with a second-order backward differencing scheme (BDF2OPT) and a timestep corresponding to an angular step of 0.25° (1440 steps per rotor revolution). Spatially, the HLLE++ (Harten, Lax, and van Leer) upwinding algorithm (Ref. 22) was used with a fifth-order spatial differencing and an improved implicit symmetric successive over-relaxation (SSOR) solver (Ref. 23) to minimize the error due to pseudo-timestepping. Additional details of the grid discretization and flow solver can be found in Thurman et al. (Ref. 6).

In both the previously-performed rotor simulation and the present airfoil simulations, a hybrid/RANS turbulence modeling framework known as DDES (delayed detached eddy simulations) (Ref. 24) was employed, using the one-equation Spalart-Allmaras model with a rotation/curvature correction (SA-neg-noft2-RC). This turbulence modeling approach is referred to as SA-DDES in this work. The SA-DDES approach has two advantages: 1) resolved turbulent fluctuations are eliminated from the simulation's boundary layer upstream of the trailing edge, and 2) laminar separation bubbles are eliminated from the simulation. A key takeaway is that SA-DDES effectively isolates BVS by eliminating TBL-TE and LBL-VS noise from the simulations. The end result is a simulation that provides a "clean" or "ideal" signal of incident surface pressures from the vortices that are shed in the near-wake. One drawback of this approach is that modeling the boundary layer as fully turbulent is likely to introduce differences in the formation and frequency of BVS when compared to BVS shed from a laminar or transitional boundary layer, but this is a limitation that is outside the scope of this study.

The rotor simulation results of Thurman et al. (Ref. 6) were revisited, with simulation parameters taken from the ITR baseline hover condition (Ref. 3), Ω = 5500 RPM, which corresponds to $M_{tip} = 0.269$ and $Re_{tip} = 1.98 \times 10^5$. Figure 3 shows the experimental data for smooth SLA (stereolithography) blades and accompanying OVERFLOW2 rotor noise predictions at an observer located a distance of 11.94R away from the rotor center and 35° below the rotor plane to match the experimental microphone location. The frequency peaks observed above 10 kHz in Figure 3 are the focus of this work.

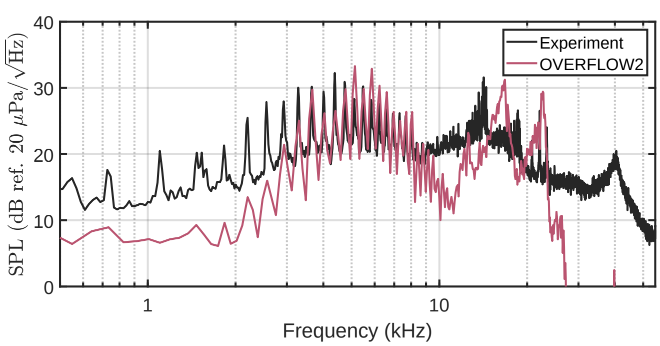

Figure 3. Far-field noise below the rotor plane (d = 11.94R, $\theta = -35°$) from experimental and simulation data. Adapted from Thurman et al. (Ref. 6).

The setup for the 2-D and 3-D airfoil simulations was designed to replicate as much of the rotor simulation as possible, including the operating conditions, grid spacing, and numerical schemes. The blade stations r = 0.55R, 0.65R, and 0.75R were chosen for these simplified simulations, and, according to Thurman et al. (Ref. 6)) should be far enough from the tip to avoid strong influence from the tip vortex roll-up and blade-wake interactions for the ITR, but far enough along the blade to be significant contributors to the overall blade self-noise spectra.

The airfoil stations were extracted from the rotor grid at the spanwise grid point nearest to the desired blade station since the surface grid points on the rotor do not perfectly align with the nominal blade stations. The nominal and actual radial stations are given in Table 2. The extracted blade surfaces were then projected onto a 2-D plane to form the airfoil surface grid. The extracted airfoil is nominally an NACA 0012 with a trailing edge (TE) thickness, h, of 0.49 mm (0.019 in.), which corresponds to $h/c = 1.54\%$. The extracted airfoils were not rotated from their geometric pitch (θ_g), which is listed in Table 2. The volume grid for each airfoil was then identically rebuilt with Chimera Grid Tools (Ref. 25) and the farfield was extended to 100 chord lengths. The final 2-D grids have 225 points around the airfoil and 151 points in the wall-normal direction. Figure 4(a) shows the near-body airfoil grid for the extracted 2-D airfoil slice for the r = 0.55R blade station. The location of a wake survey line 1.3 mm (0.051 in.) downstream of the TE is shown for reference, which matches the sampling location in Brooks, Pope, and Marcolini (Ref. 8). Figure 4(b) zooms in on the TE. Surface pressure probes on the suction and pressure sides are indicated by black dots for reference.

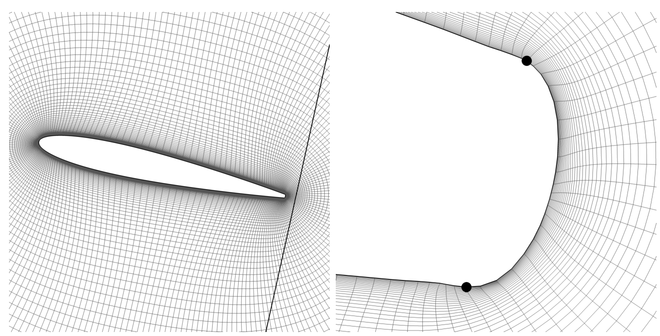

(a) Near-body grid (b) TE surface probes

Figure 4. 2-D airfoil grid extracted from the rotor simulation at r = 0.55R.

The freestream velocities, V_∞, for the three airfoil stations were computed based on the extracted radial station using $(r/R) \cdot V_{tip}$ and are listed in Table 2. Using a steady 2-D RANS simulation, the angle of attack was adjusted until the pressure distribution suction peaks matched the suction peaks extracted from the rotor simulation at the three blade station stations. The effective angles of attack for the untwisted NACA 0012's at each blade station, α_{eff}, are listed in Table 2. Although the effect of induced velocity is not explicitly accounted for in V_∞ as a simplicity, the effects are implicitly included in α_{eff} from the rotor simulation. Also listed is a condition for the r = 0.55R airfoil at the angle of attack predicted by BEMT given by Pettingill et al. (Ref. 3). This condition was included to evaluate the effectiveness of applying the 2-D approach without being able to extract α_{eff} from a rotor simulation.

With the conditions in Table 2, 2-D simulations with SA-DDES were performed with the same numerical setup as the

Table 2. 2-D airfoil simulation setup parameters.

Nominal r/R	Actual r/R at Rotor TE	V_∞ (m/s)	Re. #	θ_g (deg)	α_{eff} (deg)	α_{eff} Source	Δt / T_{BVS}	h/c (%)
0.55R	0.553	50.531	109,836	12.485	2.765	Rotor Sim.	12.85	1.54
0.55R	0.553	50.531	109,836	12.485	3.800	BEMT	12.85	1.54
0.65R	0.652	59.618	129,587	10.582	2.402	Rotor Sim.	10.89	1.54
0.75R	0.748	68.427	148,733	9.220	2.070	Rotor Sim.	9.49	1.54

rotor simulation. The same physical timestep from the rotor simulation was used for each airfoil simulation, $\Delta t_{\text{rotor}} = 1.0123 \times 10^{-5}$ seconds. The airfoil simulations were run until a steady oscillating behavior was observed in the forces, and then run for the equivalent length of time of 15 rotor revolutions, to match the number of timesteps available from the rotor simulation. Every 2 timesteps worth of data were saved from the rotor simulation. Since the 2-D airfoil simulations take up much less space, every 1 timestep was saved but the wall pressures were down-sampled to match the rotor simulations when performing the spectral post-processing. Farfield noise was predicted with these unsteady surface pressures using Farassat's Formulation 1A (F1A), an approach to solving the Ffowcs-Williams and Hawkings (FW-H) equations (Ref. 26). All spectral processing of acoustic pressure time-histories was performed using a Hanning window with a 75% overlap.

Assuming a shedding frequency of St = 0.1 (Refs. 7, 8), based on the velocity at each station, Table 2 shows the time resolution of the simulation based on the BVS period (timesteps per BVS period, T_{BVS}). Ideally, more timesteps would be used to discretize the vortex shedding, so it is possible that the BVS events on the rotor are slightly under-resolved in time. However, by keeping identical grid spacings, numerical schemes, timestep sizes, and data sampling rates the same, a direct comparison can still be made between the 2-D airfoil and 3-D rotor simulations to isolate and understand the effects of 3-D flow effects on the BVS shedding frequency even though neither the 2-D nor 3-D simulations is converged to the "true" frequency.

RESULTS

The results section is organized as follows: rotor flowfield features, farfield noise, and wall pressure spectra are first investigated to identify BVS and other noise sources including blade-wake interaction (BWI), blade-wake backscatter (BWBS), and tip vortex formation (TVS) noise. A single rotor blade station, r = 0.55R, is then studied to identify BVS noise through an analysis of wall pressure spectra. Then, 2-D airfoil simulations are performed at freestream conditions corresponding to three rotor blade stations: r = 0.55R, r = 0.65R, and r = 0.75R. Wall pressure spectra from the 2-D airfoils are then compared to wall pressure spectra from the extracted rotor stations to identify trends. 3-D airfoil simulations are briefly discussed, including comparing wall pressure spectra to the other two simulation methods. Finally, farfield BVS noise is predicted from the airfoil simulations.

Rotor Flowfield Features

Prior to a discussion of the predicted rotor noise spectra, a brief investigation of relevant flowfield features is warranted to identify which of these flow features interfere or overlap with BVS along the blade. Using an isosurface of Q-criterion colored by spanwise vorticity, Figures 5(a) and (b) show the shed vortical structures in the wake of one ITR blade including the von Kármán vortex street at the blade's trailing edge over a large portion of the span. Red (positive spanwise vorticity) and blue (negative spanwise vorticity) reveal wake vortices shed with alternating rotation directions. Figure 6 shows section cuts at the TE (trailing edge) at two blade stations, r = 0.55R and 0.75R, at the same instance in time. Contours of spanwise vorticity confirm the presence of vortices shed from the suction side and pressure side at each blade station, indicating BVS.

Viewing the same isosurface of Q-criterion from above the suction side of the blade, Figure 5(b) labels blade stations at 0.1R increments. The downstream paths of the vortices are skewed by either the rotational flowfield or crossflow. At r = 0.80R and outboard, the convection direction of the vortices shifts, and a disruption in the shed vortex wake can be seen at r = 0.85R. These disturbances are likely caused by the previous blade's vortex core and surrounding wake field (Ref. 6). The interaction of the previous blade's vortex and wake is sometimes referred to in the literature as perpendicular blade-vortex interaction (BVI). For the rest of this work, this interaction will simply be referred to as blade-wake interaction (BWI).

The influence of BWI is visualized via vorticity magnitude plotted on planes slicing through the blade's leading edge (LE) (Figure 7(a)) and trailing edge (Figure 7(b)). Black contours indicate regions of high vorticity. The tip vortex (also visualized in Figure 5) can be seen rolling up and interacting with the trailing edge at least at r = 0.95R and outboard. The preceding blade's vortex core is observed to pass under the blade and covers approximately from r = 0.85R to 0.95R, with the center approximately at r = 0.90R. Figure 7(b) shows the current blade slicing through the vortex wake field surrounding the previous blade's vortex core. Due to the rotation of the previous blade's vortex and surrounding wake field, there are likely significant downwash effects between r = 0.80R and 0.85R and significant upwash effects from r = 0.90R to 0.95R (Ref. 6). The vortex wake field is also likely shifting the downstream path of the shed TE vortices in Figure 5(b). Furthermore, Thurman et al. (Ref. 6) identified the presence of turbulence in the wake field surrounding the previous blade's

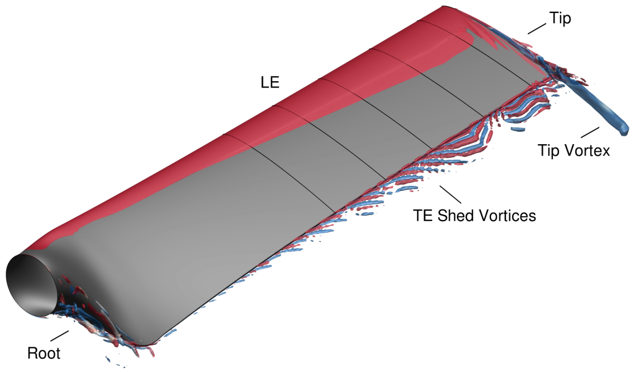

(a) Isometric view

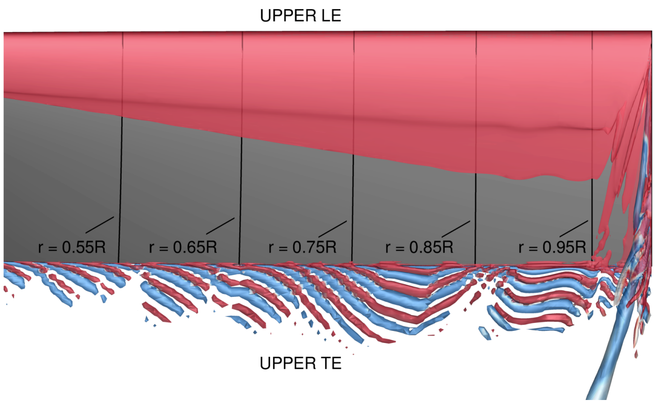

(b) Top-down view

Figure 5. Q-criterion of the rotor wake, colored by spanwise vorticity (red = positive rotation, blue = negative rotation).

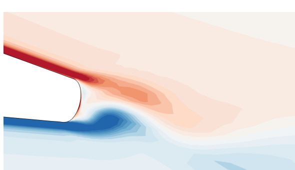

(a) r = 0.55R

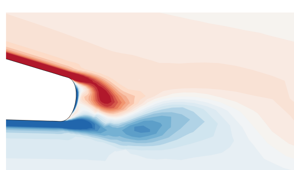

(b) r = 0.75R

Figure 6. Spanwise vorticity contours at the trailing edge for two stations from the rotor simulation (red = positive rotation, blue = negative rotation).

vortex core. This turbulence impinges on the leading edge of the current blade, convects over the chord, and then interacts with the current blade's trailing edge to generate BWBS (blade-wake back-scatter), a type of BWI. With knowledge of the spanwise location of the tip vortex roll-up and BWI events, noise sources along the blade can be investigated more clearly.

Rotor Noise Sources

Peaks in the predicted farfield rotor noise spectra were investigated by computing the noise generated by several spanwise stations and identifying their contribution to the blade's spectra. Short spanwise sections were formed every 0.05R blade station from r = 0.50R to 0.95R by selecting two neighboring

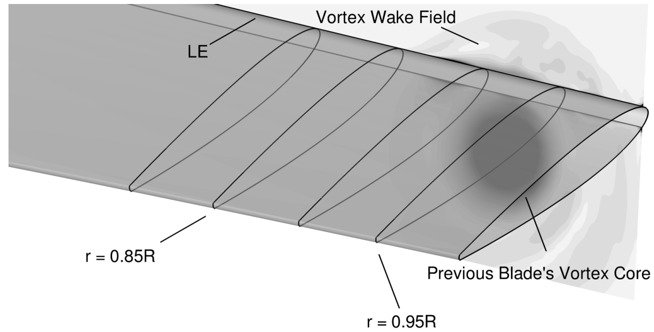

(a) Spanwise plane at LE

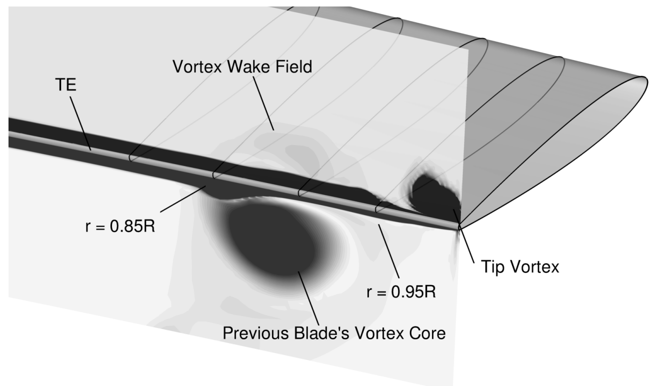

(b) Spanwise plane at TE

Figure 7. Isosurfaces of vorticity magnitude visualized on spanwise planes (black = high vorticity).

spanwise grid points from the surface grid. The points were chosen to encompass the targeted radial station. Figure 8(a) shows the spanwise sections imposed on a top-down view of the blade surface for reference. It should be noted that, due to the decreasing spanwise grid spacing towards the blade tip, these small spanwise sections do not have equal area. Time-varying pressures on each of the sections were extracted from one blade over 15 rotor revolutions, and the farfield noise was computed with ANOPP2's Formulation 1A solver (Ref. 26) (F1A) using an impermeable data surface for each spanwise section. The observer position was chosen to be 11.94 R away and aligned above the rotor on the rotor's axis to eliminate Doppler shift and isolate nonperiodic noise sources. For comparison, the noise from all blade stations for one entire blade was also calculated. The acoustic pressure time histories at the observer were then processed to produce the farfield spectra. The frequency bin width for this analysis (and all farfield spectra in this work) was chosen to be 132 Hz to increase the number of effective averages in the data to smooth out the spectra, which is recommended for this relatively short signal length.

Figure 8(b) shows the contribution of individual spanwise blade stations to the farfield noise spectra of one blade, with colors corresponding to the spanwise stations in Figure 8(a). The frequency range is focused only on the portion of the high-frequency broadband spectra above 10 kHz and below 24 kHz where strong peaks are observed in Figure 3. Four distinct regions were identified and highlighted in Figure 8(c) to aid in analyzing the blade's component noise sources. All four regions must be discussed briefly to help identify which peaks, if any, correspond to BVS and to rule out frequency contributions from non-BVS noise sources.

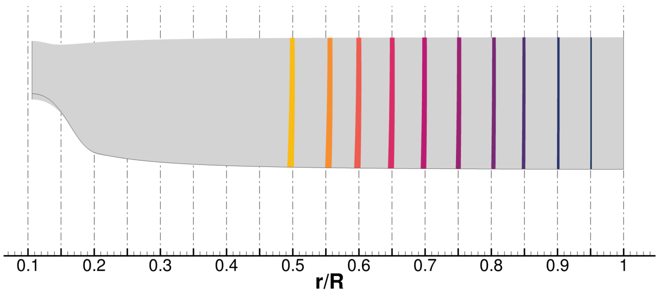

(a) Selected spanwise blade sections

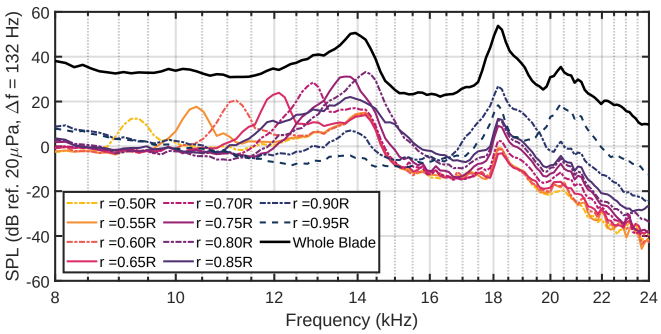

(b) Noise from spanwise blade stations

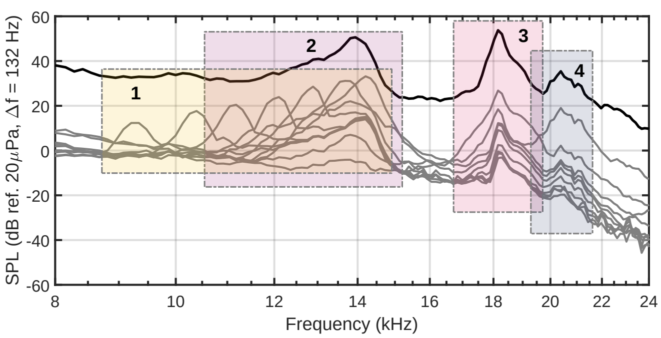

(c) Four noise Regions

Figure 8. Farfield noise predicted for one blade and for selected blade stations. Four noise Regions are labeled.

Region 1 in Figure 8(c) appears to correspond to a noise source that increases in frequency with increasing blade station and appears to be responsible for a slight spectral hump from 10 kHz to 15 kHz. Since the velocity component tangential to the rotation direction increases with radial station, the noise source leading to peaks in Region 1 likely scales with velocity. The amplitude of the noise source in Region 1 also increases with radial station and velocity. These sources do appear to contribute to the overall spectral shape, especially in the 10–14kHz range. It will be demonstrated in later sections that the noise sources in Region 1 correspond to BVS.

Three significant peaks are observed in the whole blade spectra in Figure 8(b). From the farfield spectra, Region 2 corresponds to an approximately 14 kHz peak with the strongest amplitude at r = 0.80R. This peak frequency is not constant at each spanwise station though, and instead the spectra from each station form a broader asymmetric spectral hump at frequencies between 12 kHz–14 kHz. Region 3 corresponds to an approximately 18 kHz peak with the strongest amplitude at r = 0.90R. Region 4 corresponds to an approximately 20.5 kHz peak with the strongest amplitude at r = 0.95R. These three peak frequencies can be observed in the spectra at each blade station, but with the amplitude decreasing with increasing distance from the peak amplitude blade station, which is suggestive of noise sources that occur at specific blade stations and then radiate strongly to other blade stations. The cumulative effect for the whole blade is peaks in the rotor spectra at these frequencies.

It is suggested by the brief analysis that follows that BWBS noise at the outboard blade stations is responsible for the peaks in Regions 2, 3, and 4. Region 2 could be a combination of BVS and BWBS, while Region 4 could have some influence by tip vortex formation (TVF) noise, a rotor broadband self-noise source (Ref. 8).

To confirm that the frequency peaks in Regions 2 – 4 are noise sources localized to the outboard blade stations, frequency metadata from F1A was extracted from the unsteady blade surface pressures. The data from one revolution was processed through a fast Fourier transform (FFT) as a single bin, resulting in bin width of 92 Hz. The unsteady pressure loading term of F1A was visualized to identify regions of the blade where strong pressure fluctuations are occurring at a discrete frequency. In other words, regions of the blade with high values of unsteady loading are experiencing strong pressure fluctuations at the given frequency. In this manner, noise peaks in the farfield observer spectra may be located on the blade for a known frequency of interest.

Figure 9 shows contour plots of F1A's unsteady loading term on the suction and pressure sides of the blade at discrete frequencies to determine the location on the blade that corresponds to the most strongly radiated farfield noise. The suction side surface is shown on the top and the pressure side surface is shown below in each sub-figure. The selected frequencies approximately correspond to the peaks of identified Regions 2–4 in Figure 8(c): 13.883 kHz for the peak in Region 2, 18.205 kHz for the peak in Region 3, and 20.412 kHz for the peak in Region 4.

The peak in the unsteady pressure contour for a frequency of 13.885 kHz (Figure 9(a)) occurs at the trailing edge between r = 0.75R and 0.80R and appears to radiate upstream and inboard on both the suction and pressure sides. The fact that each blade station has some contribution from the range of frequencies between 12 kHz to 14 kHz in the spectra of Figure 8(b) adds to the argument that this is a strongly radiating noise source. An instantaneous snapshot of unsteady pressure loading from F1A was extracted and plotted in Figure 10 to confirm that strong pressure waves originate at the trailing edge between r = 0.75R and 0.80R and propagate inboard and toward the leading edge. Arrows indicate the propagation direction, identified through time animation, for reference. Thurman et al. (Ref. 6) identified this efficiently radi-

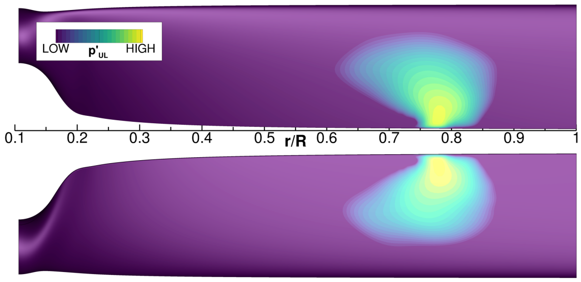

(a) 13.885 kHz, Region 2

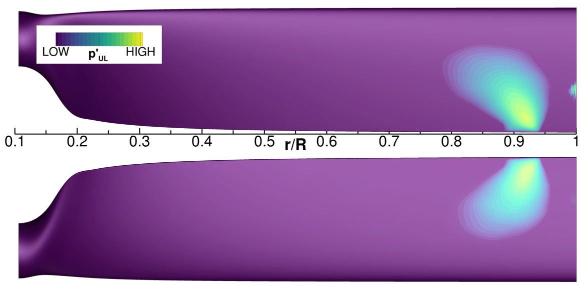

(b) 18.205 kHz, Region 3

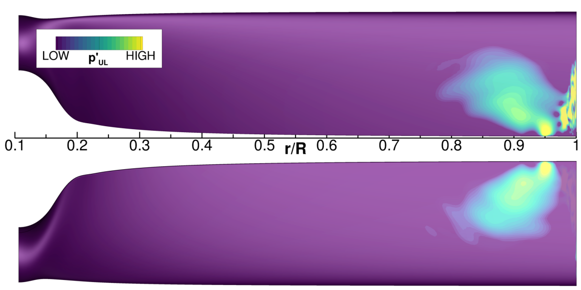

(c) 20.412 kHz, Region 4

Figure 9. Contours of the unsteady loading term from F1A at peak frequencies in Regions 2-4. The suction side is shown on top of the pressure side.

ating noise source as BWBS.

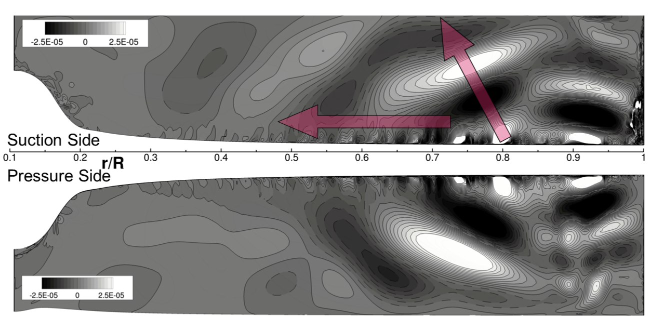

Figure 10. Instantaneous unsteady pressure loading from Farassat's Formulation 1A. Adapted from Thurman et al. (Ref. 6).

Small unsteady pressure hot spots can also be observed at the TE from r = 0.50R to 0.75R in Figure 10, and are likely BVS given that these do not appear to radiate strongly. Figure 5(b) shows that vortex structures indicative of BVS form at the TE between r = 0.50R and 0.80R. The vortex structures at r = 0.80R appear slightly stronger and more coherent in the spanwise direction than structures that are further inboard. While it is possible that the downwash and upwash of the previous blade's vortex wake field is augmenting the BVS at r = 0.80R, BVS is not likely the source of the strong unsteady pressures between r = 0.75R and 0.80R since BVS is not an efficient radiator at other inboard blade stations. It is therefore reasonable to conclude that BWBS is the dominant noise source leading to the 13.885 kHz peak in Region 2 of Figure 8(c).

Figure 9(b) shows strong pressure loading at the trailing edge between r = 0.90R and 0.95R at the frequency of 18.205 kHz, confirming the findings from Figure 8(c). These blade stations are likely the region of strongest upwash due to the BWI event. Again, the unsteady loading in Figure 10 shows strong fluctuating pressures at the TE that appear to radiate, although the direction of wave radiation is difficult to identify. Thurman et al. (Ref. 6) also identified this noise source as BWBS. In addition, slight unsteadiness at the leading edge can be observed in Figure 10 which is more suggestive of blade-wake turbulence and BWBS. Therefore it is reasonable to conclude that the 18.205 kHz noise source is BWBS.

Figure 9(c) shows strong pressure loading at the trailing edge at r = 0.95R that also appears to propagate inward. Additionally, contour hot spots at the tip visualize the tip-vortex roll-up occurring at r = 0.95 and outboard. It is possible that the noise peak at the frequency of 20.412 kHz (Region 4 in Figure 8(c)) is due to a combination of blade wake and tip-vortex formation, which suggests BWBS and TVF noise.

Conclusively demonstrating the existence of BWBS, BWI, and TVF noise falls outside the scope of this work and will be left to future investigations. However, from the above analysis, it can be concluded that blade-wake effects are present and are likely influencing wall pressures on the blade outboard of r = 0.75R, making it difficult to separate BVS from other noise sources at those outboard stations. Therefore, the remainder of this work will focus only on BVS at blade stations inboard of r = 0.75R.

BVS Noise in Region 1 According to Brooks and Hodgson (Ref. 7) and Brooks, Pope, and Marcolini (Ref. 8), the BVS shedding frequency scales with a Strouhal number based on trailing edge thickness,

$$St = \frac{f \cdot h}{V_\infty} = \frac{f \cdot h}{\Omega \cdot r}, \tag{1}$$

where f is the BVS shedding frequency, h is the thickness of the blunt trailing edge, and V_∞ is the freestream velocity, which is taken as the sectional velocity $(\Omega \cdot r)$ in this work. Although the BVS Strouhal number is expected to vary slightly, a nominal value of 0.1 is used to identify BVS along the blade (Refs. 7, 8). BVS noise along the rotor blade is studied in this section and includes a detailed look at the r = 0.55R blade station, which was chosen because BVS at this station is easily identifiable and occurs at frequencies separate from other noise sources occurring further outboard.

The spectral peaks in Region 1 of Figure 8(b) increase in amplitude and frequency with increasing radial station and increasing tangential velocity, suggesting a Strouhal number scaling. The increasing peaks only cover a narrow frequency range for each blade station, which is expected of BVS. The stacking of the spanwise varying BVS spectral peaks from Region 1 appear to lead to the increasing slope of frequencies toward 14 kHz in the whole blade spectra.

Figure 11 shows the farfield noise for each of the 0.05R blade stations with a Strouhal number frequency scaling (see Eqn. 1), where the freesteam velocity is taken as the sectional tangential velocity at each blade station due to rotation, $V_r = \Omega \cdot r$. The general trend is that the peaks align to approximately 0.1 for stations from r = 0.55R to 0.75R. The peaks appear to shift to lower St closer to the blade tip. The peak at r = 0.80R could be BVS, but the analysis from the previous sections makes this inconclusive. The peaks from sections r = 0.85R and 0.90R do not align with the St = 0.1 and are therefore not caused by BVS. Similarly, the spectra from r = 0.95R can be removed from analysis because of the influence of the tip vortex roll-up. It should be noted that the blade span area is included in the F1A integration for farfield noise and so the exact amplitudes levels may not be directly comparable to one another because the blade station spanwise widths are not identical. However, similar trends are expected.

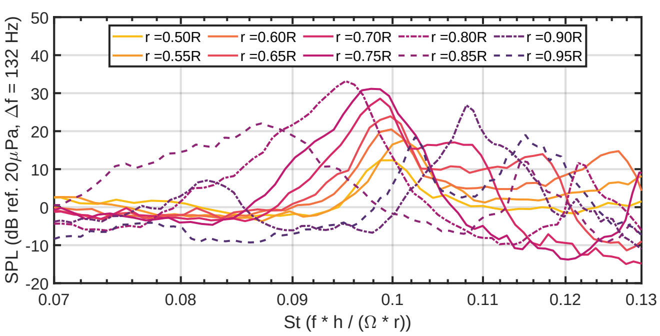

Figure 11. Farfield noise from spanwise blade stations for one rotor blade scaled by Strouhal number.

BVS generates significant pressure fluctuations that are localized at the trailing edge (Ref. 7), and it is expected that this shedding would be highly coherent between the suction and pressure sides. Contours of the unsteady loading term from F1A are plotted in Figure 12 at an isocontour of Strouhal number = 0.1, calculated from frequency using Equation 1. The contours show regions on the blade that radiate farfield noise at nominal BVS frequencies along the span. BVS peaks appear as contour hot-spots along the trailing edge from r = 0.50R to 0.75R. The localized nature of these hot-spots to the TE helps confirm that these are due to TE vortex shedding.

However, streaks are noted in Figure 12 along the mid-chord of the blade from r = 0.675R to 0.80R and at 0.975R. These streaks likely indicate the presence of a non-BVS noise source

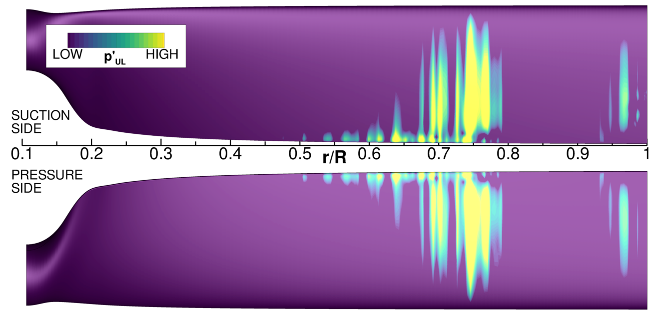

Figure 12. Isosurface of St = 0.1 colored by the unsteady loading term from F1A using frequency metadata.

like BWBS that radiates to the mid-chord at similar frequencies to the expected BVS frequency. If BVS and a non-BVS noise source generate wall pressure fluctuations at similar frequencies at a selected blade station, the two similar frequencies will scale to approximately the same Strouhal number since the sectional velocity is the same. Therefore, it is likely that streaks on the mid-chord do not correspond to BVS. Since the image is an isocontour of a frequency with a bin width of 92 Hz, only unsteady loading that corresponds to the spanwise-varying shedding frequency of $\pm$ 46 Hz is shown.

A spectral analysis was performed on wall pressure fluctuations from sensors as close to the trailing edge as possible (see Figure 4(b)) on the suction side and pressure side of the airfoil. The spanwise locations correspond to the same stations used to extract the surface pressures for the farfield noise. The spectral processing of the rotor data was carried out at a frequency bin width of 128.9 Hz (rounded to 129 Hz) to increase the amount of effective averages with the relatively short time history.

Figure 13 shows suction side TE wall pressure spectra (WPS) scaled by Strouhal number at 0.05R increments along from r = 0.50R to 0.75R. The presence of the main BVS tone is observed in the narrow spectral peaks mostly centered around St = 0.1. For the two outboard stations, r = 0.70R and 0.75R, the peak frequency has shifted closer to 0.097. The reason for the shift is unknown and requires further study. The presence of the second harmonic of the shedding frequency can be observed at approximately St = 0.2. For strong vortex shedding, it is plausible for harmonics to be observed in the WPS without the presence of freestream turbulent fluctuations, which are not expected in this simulation due to the RANS-modeled boundary layer. Together with Figure 12, Figure 13 demonstrates that the TE WPS shows a large amplitude peak corresponding to BVS. This peak can be used to identify the BVS shedding frequency at each blade station.

BVS at the r = 0.55R Blade Station This section further demonstrates extracting the BVS frequency from TE WPS from the r = 0.55R blade station through farfield noise unsteady loading on the surface, WPS, coherence, and phase information. The r = 0.55R blade station is chosen because the BVS peak, 10.393 kHz in Figure 8(b), is isolated from

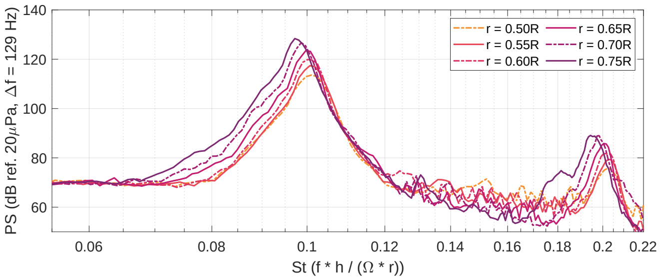

Figure 13. Trailing edge wall pressure spectra scaled by blade station Strouhal number.

the buildup of frequencies around 14 kHz corresponding to Region 2.

The farfield noise spectra from the small spanwise section centered on the r = 0.55R blade section is shown in Figure 14. Three main peaks are labeled: Peak 1 = 10.393 kHz, Peak 2 = 14.207 kHz, and Peak 3 = 18.154 kHz. Contours of unsteady pressure loading at frequencies corresponding to each peak are shown in Figures 15(a) – (c). Contour levels are adjusted for each image, given the variation in amplitude in Figure 14.

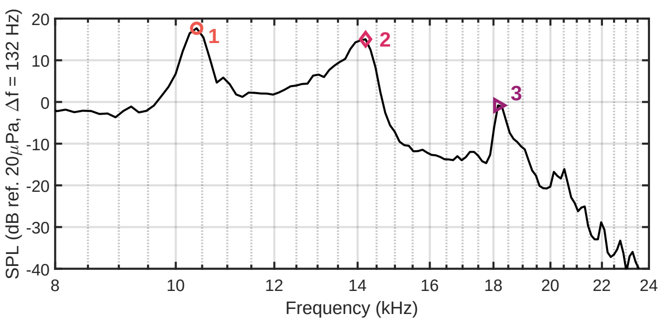

Figure 14. Farfield noise for small spanwise section at r = 0.55R.

The suspected BVS frequency, Peak 1, shows up as high unsteady pressure loading localized to the trailing edge in Figure 15(a) which is expected of BVS. Figures 15(b) and (c) for peaks 2 and 3 show high unsteady pressure loading only along the mid chord, and more on the suction side than the pressure side. These contours are consistent with previous analysis of these two frequencies that suggests a noise source originating at another blade station and radiating to the r = 0.55R station. This analysis gives confidence that the 10.393 kHz frequency, the largest amplitude peak in the WPS, is caused by a BVS source and the other peaks are from non-BVS sources.

BVS at Three Blade Stations Continuing with the investigation of BVS, TE WPS from the suction and pressure surfaces were extracted from the probe locations shown in Figure 4(b) for the three blade stations, r = 0.55R, 0.65R, and 0.75R. The discussion focuses on the r = 0.55R blade station, but can be applied to all three stations.

Figure 16(a) shows autospectra for the suction and pressure sides. The frequency axis is scaled by Strouhal number, using the velocity at each station (50.532 m/s at the extracted rotor

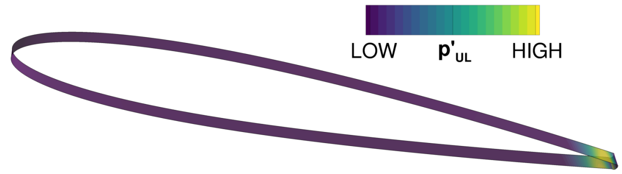

(a) 10.393 kHz, Peak 1

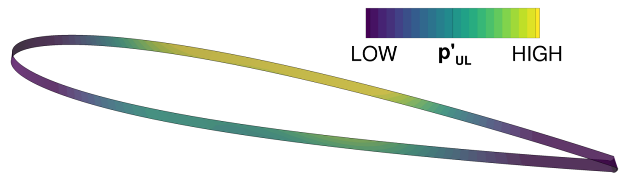

(b) 14.207 kHz, Peak 2

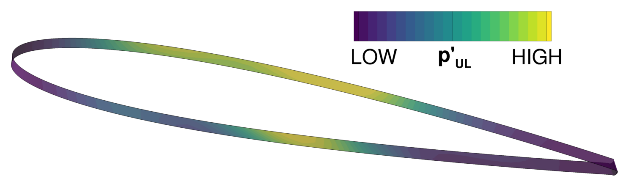

(c) 18.154 kHz, Peak 3

Figure 15. Isosurfaces of frequency colored by the F1A loading pressure term at the r = 0.55R blade station.

station, r = 0.553R). BVS shedding is identified by the presence of a strong WPS peak the shedding frequency at St = 0.1. The second harmonic is observed at approximately St = 0.2. The spectra display other small peaks that could be related to noise sources from Regions 2–4. Cross spectra between the suction and pressure side (see Figure 16(b) where the "SS x PS" in the legend indicates a suction side and pressure side sensor pair) confirm that both suction and pressure side signals are correlated at this peak frequency.

Additionally, the suction and pressure side WPS should be coherent at the shedding frequency because they are experiencing effects of the same BVS event. Confirming this, the suction and pressure side signals show near-perfect coherence at the peak frequency (Figure 16(c)). Other frequencies besides the BVS peak and the second harmonic appear to show non-zero coherence between the two sensors, but these do not correspond to large peaks in the TE WPS other than the second harmonic frequency and are therefore not caused by BVS. It is possible that these coherent frequencies are related to BWBS felt on both the pressure and suction sides or that the flowfield is artificially coherent without the randomness of turbulent fluctuations in the boundary layer to decorrelate the flow.

Since BVS is caused by the alternating shedding of suction side and pressure side trailing edge vortices, phase information should reveal an out-of-phase relationship between suction side and pressure side surface pressure fluctuations at the

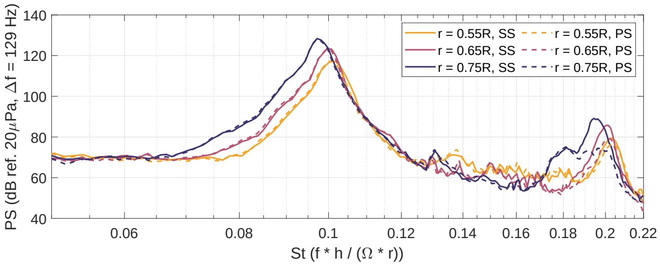

(a) Autospectra

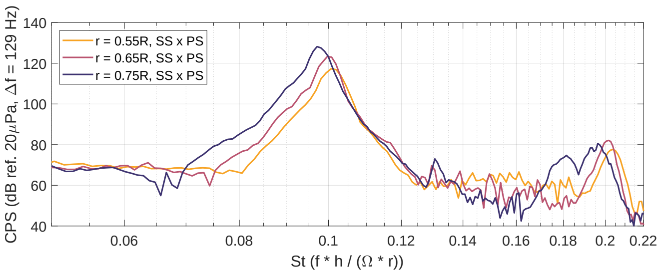

(b) Cross spectra between SS and PS

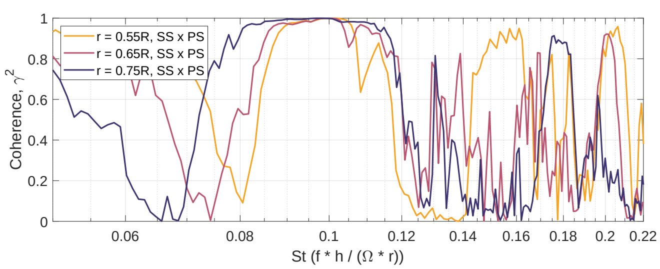

(c) Coherence between SS and PS

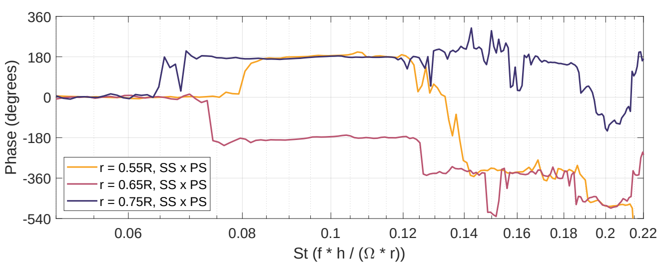

(d) Phase between SS and PS

Figure 16. Wall pressure spectra at the TE from three rotor stations at r = 0.55R, 0.65R, and 0.75R. Frequency is scaled by Strouhal number. (a) Autospectra, (b) cross spectra, (c) coherence, and (d) phase are shown for suction side (SS) and pressure side (PS) sensors.

TE (Ref. 9). The phase relationship at the peak frequency is approximately 180 degrees (Figure 16(d)), which confirms out-of-phase vortex shedding.

Collectively, the farfield noise, WPS spectral peaks, and WPS coherence and phase information all help to confirm the existence of BVS at the trailing edge for the r = 0.55R blade station. This method of analysis can serve as an example technique to confirm BVS at other spanwise stations, specifically r = 0.65R and 0.75R as shown in Figure 16.

By applying a similar analysis to r = 0.65R and 0.75R using the data shown in Figure 16(a) – (d), BVS is confirmed at these blade stations. It should be noted that the peak frequency of the WPS at r = 0.75R does not collapse exactly to St = 0.1. As previously mentioned, the blade wake appears to influence the outer blade stations, potentially even r = 0.75R. An increase in the tangential velocity at this station from blade-wake downwash would decrease the Strouhal number scaling for a given shedding frequency. Although not presented here for brevity, wall pressure fluctuations at the leading edge of r = 0.75R did appear to confirm the presence of turbulent fluctuations in the blade wake. An analysis of Figure 16 of peak WPS, coherence, and phase, including a peak at the second harmonic frequency, suggests that BVS is occurring at the trailing edge at r = 0.75R. Flowfield visualizations (Figure 6) confirm the existence of vortices at the TE at this location. Therefore it is reasonable to conclude that BVS does exist at the r = 0.75R station, but that the freestream velocity and shedding frequency might be influenced by blade-wake effects.

Spectral Width of BVS Peaks A tonal peak is usually expected for an oscillating vortex shedding at a fixed frequency. However, in both the rotor farfield and WPS spectra, the BVS peak is actually more of a spectral "hump". The question remains as to why the BVS spectral peaks are not sharper.

The width of the spectral "hump" is most likely due to the fact that the sectional blade velocity varies along the blade as $V_r = \Omega \cdot r$. Figure 17 shows the farfield noise for r = 0.55R processed at two bin widths, 132 Hz and 33 Hz. For the 132 Hz bin width, the resulting random autospectral uncertainty is +1.435 dB and -1.676 dB. For the 33 Hz bin width, the random autospectral uncertainty is higher (+2.877 dB and -4.055 dB) due to the decreased number of effective averages. Even though the amplitude uncertainty is greater for the 33 Hz bin width processed data, two additional "humps" are observed within the first "hump". These two "humps" correspond to the spanwise change in sectional velocity.

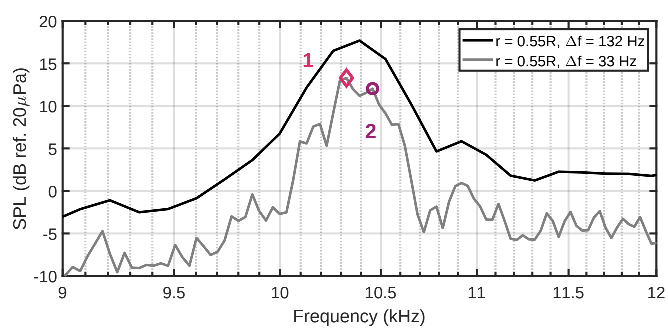

Figure 17. Farfield noise spectra for the r = 0.55R rotor station processed with two different frequency bin widths.

If BVS is present along the blade, and if the trailing edge thickness is constant (as is the case for the ITR), then the shedding frequency can be expected to increase towards the blade tip. Recall that when analyzing the contribution of each blade station to the overall blade spectra, each spanwise section was taken from only two points on the rotor blade surface. In Figure 17, the two distinct frequency "humps" appear to be from the inboard and outboard blade stations that make up the short spanwise blade section at r = 0.55R. To confirm this, the unsteady loading term from F1A frequency metadata at r = 0.55R is shown in Figure 18 at the two peak frequencies from Figure 17. Figure 18(a) corresponds to 10.326 kHz, and a contour hot spot is observed closer to the inboard section (closest to the viewer). Similarly, Figure 18(b) corresponds to 10.485 kHz and a contour hot spot is observed closer to the outboard section (furthest from the viewer).

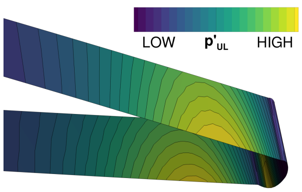

(a) 10.326 kHz

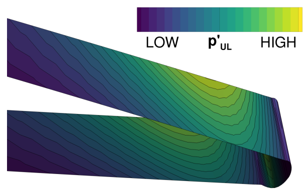

(b) 10.485 kHz

Figure 18. Frequency isosurfaces at the trailing edge, (a) 10.326 kHz, (b) 10.485 kHz, colored by the F1A unsteady loading pressure term.

To further confirm this spanwise variation of BVS frequency, suction side TE WPS from 3 adjacent grid points on the rotor centered at r = 0.55R are plotted in Figure 19. The increasing spanwise station corresponds to an increasing peak frequency. Additionally, coherence between the inboard pair (r = 0.542R and 0.549R) and the two outboard pair (r = 0.549R and 0.556R) also demonstrate an increasing frequency towards the outboard station, confirming the spanwise variation in BVS frequency.

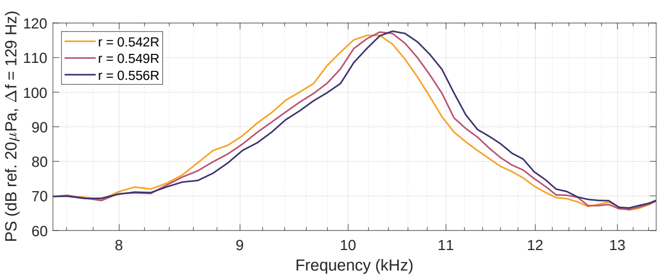

(a) Autospectra

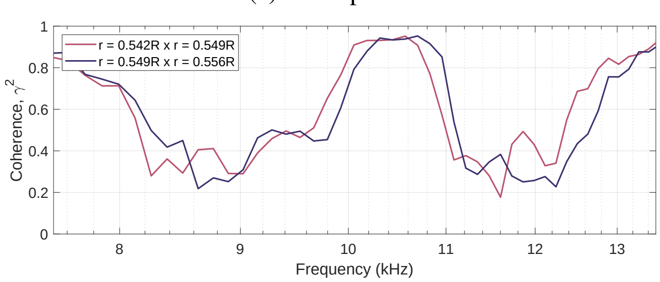

(b) Coherence between Spanwise-Adjacent Stations

Figure 19. Trailing edge WPS at three adjacent blade stations centered at r = 0.55R.

From this analysis, it can be concluded that the BVS frequency is generally increasing along the span. A likely scenario is that BVS occurs in small spanwise coherent patches along the blade and that WPS extracted at one station is likely to "feel" the presence of pressure fluctuations from the neighboring blade stations that are occurring at slightly different frequencies, resulting in a spectral "hump" rather than a clean tonal peak.

To demonstrate this, an example WPS spectra was generated for 5 adjacent spanwise blade stations, each separated by 0.005c (0.001R), with the "target" station in the center (r = 0) and two stations inboard and outboard of the central station. BVS was assumed to occur at each station at St = 0.1, with the frequency varying with $\Omega \cdot r$ as it would with a rotor. The WPS was given a simple Gaussian shape. Figure 20 shows an example of the wall pressures (hydrodynamic or acoustic) that are "felt" or "sensed" at the central blade station (the station of interest) by BVS events occurring at the inboard and outboard adjacent spanwise stations. The amplitudes were decreased to either side of the central station to indicate the drop in pressure over the spanwise separation between stations. The frequencies are Strouhal scaled by the velocity of the center station to indicate that BVS frequency increases along the span. The dashed black line shows the overall spectra summed up at the center station, which is meant to represent the WPS at one station with influence from BVS events at adjacent blade stations. The resulting shape is a spectral "hump" rather than a peak. It is possible to see that if BVS was stronger at one off-center station, the influence could be "felt" at the center station. Given that the spanwise variation in BVS frequency on the ITR has already been demonstrated in previous sections, this example is a possible explanation for the wide spectral "hump" observed in the rotor WPS and farfield noise.

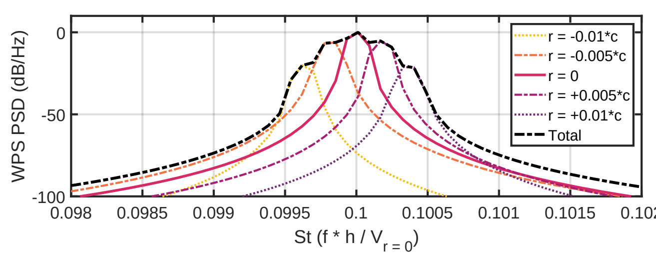

Figure 20. Fabricated WPS demonstrating the spanwise variation in BVS shedding frequency and the wide resulting spectral peak at the center spanwise station.

2-D Airfoil Simulations

The above analysis demonstrates that BVS exists on the ITR rotor and that the peak frequency increases radially with sectional velocity. With this knowledge, 2-D simulations were performed at flow conditions corresponding to three rotor stations: r = 0.55R, 0.65R, and 0.75R. The goal is to determine if the trends for peak shedding frequency and amplitude can be predicted with a simplified approach using a 2-D airfoil simulation instead of a full 3-D rotor simulation. Freestream conditions for each of the three blade sections are given in Table 2.

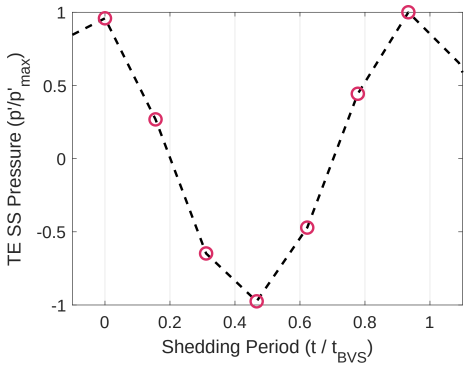

(a) Pressure fluctuations per BVS period

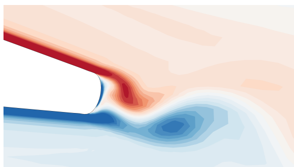

(b) $t/t_{\mathrm{BVS}} = 0.00$

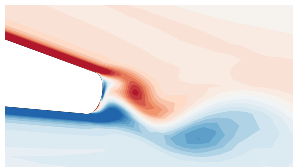

(c) $t/t_{\mathrm{BVS}} = 0.15$

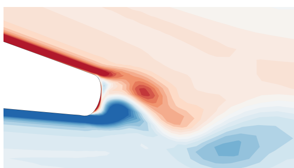

(d) $t/t_{\mathrm{BVS}} = 0.31$

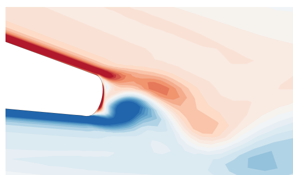

(e) $t/t_{\mathrm{BVS}} = 0.47$

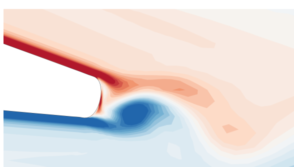

(f) $t/t_{\mathrm{BVS}} = 0.62$

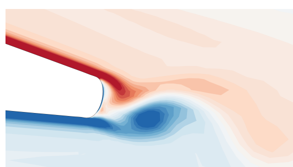

(g) $t/t_{\mathrm{BVS}} = 0.78$

Figure 21. Time-varying spanwise vorticity contours at the trailing edge of the r = 0.55R airfoil (red = positive rotation, blue = negative rotation).

Visualization of Vortex Shedding Spanwise vorticity (along the axis of the 2-D BVS vortices) is plotted in the TE near-wake in Figure 21 for the r = 0.55R 2-D airfoil simulation. An example shedding period is shown in Figure 21(a), with pressure from the suction side sensor non-dimensionalized by the maximum level for simplicity. Data is shown every two timesteps to represent the data from the rotor simulation. Figures 21(b) – (g) show the time development of the BVS shedding process at corresponding points in the shedding cycle indicated by circles in Figure 21(a). As listed in Table 2, the rotor timestep corresponds to 12.85 timesteps per BVS shedding period in this case. As mentioned previously, this temporal discretization is coarse and may indicate the need to reduce the timestep in future simulations to better resolve the shedding period.

Both suction and pressure side shed vortices demonstrate classic Kelvin-Helmholtz vortex roll-up and shedding. The red (positive rotation) and blue (negative rotation) vorticity contours indicate that vortices of opposite rotation are shed from suction and pressure sides as expected. The vortex shed from the pressure side appears larger in diameter and stronger than the vortex shed from the suction side, a behavior that is likely due to the slight effective angle of attack of the airfoil, with the pressure side surface experiencing greater flow turning leading to a stronger vortex roll-up. A positive pressure pulse on the suction side appears to correspond with the shedding of a vortex from the suction side, and the same is true for the vortex shed from the pressure side.

For all three airfoils, Figure 22 depicts the same spanwise vorticity contours at the approximate trough of each BVS period. The contour levels are the same between all three and the stronger (darker) contours on the r = 0.75R station suggests that the relative strength of the BVS event increases along the span. Vortex roll-up behavior in the near-wake appears qualitatively similar to shedding observed from rotor stations (Figure 6). The vortices dissipate quickly in the wake due to the coarsening near-wake grid. The existence of BVS shedding in multiple simulations confirms the ability of SA-DDES to model BVS with 2-D airfoil simulations.

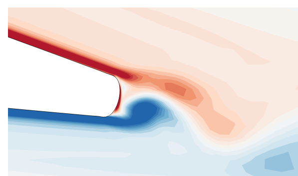

(a) r = 0.55R

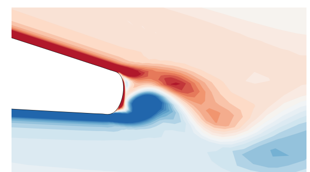

(b) r = 0.65R

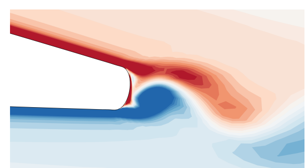

(c) r = 0.75R

Figure 22. Spanwise vorticity contours at the trailing edge for the 2-D airfoil simulations (red = positive rotation, blue = negative rotation).

Comparison to Rotor Wall Pressure Spectra Given that BVS generates pressure fluctuations at the TE, comparing wall pressure spectra between the three 2-D airfoil simulations and their corresponding rotor stations gives the best indication of the differences between simulation methods. This section compares both the frequency and peak amplitude of the BVS shedding.

Wall pressures were extracted at the surface probes shown in Figure 4(b), which correspond to x/c = 0.995 for each airfoil station. For simplicity, only WPS from the suction side TE are used to compare to the rotor WPS. The BVS frequency is identified by finding the maximum amplitude in the WPS spectra.

Figure 23 shows the suction side TE WPS for the three rotor blade stations and the three 2-D airfoils. Peak frequencies and amplitudes are listed in Table 3 for convenience. The BVS frequency predicted by the 2-D airfoil simulations varies by 100

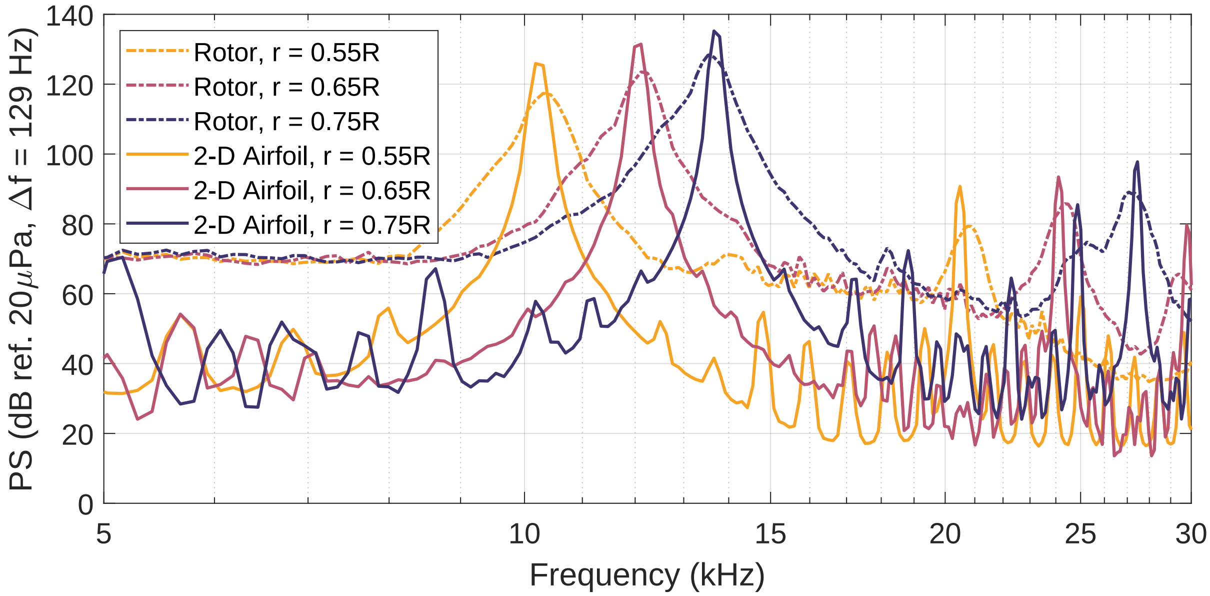

Figure 23. Wall pressure spectra at the suction side TE from r = 0.55R, 0.65R, and 0.75R for both 2D airfoil and rotor simulations.

to 200 Hz from the 3-D rotor simulations at each of the three stations, which is less than a 2% difference. It should be noted that the peak frequencies are plotted on a 132 Hz basis, so this suggests that the peak BVS is predicted within one or two frequency bin widths at this frequency resolution. The increase in shedding frequency with increasing radial station and increasing sectional velocity is predicted well. For r = 0.55R and 0.65R, the frequency of the 2-D airfoil simulation underpredicts the peak frequency from the rotor simulation. For the r = 0.75R station, the 2-D airfoil station overpredicts the shedding frequency compared to the rotor simulation. This slight deviation in trend could indicate that 3-D or blade-wake effects are influencing the rotor WPS more here than previously thought. The second harmonic of each frequency is also observed in the spectra. Additional small peaks can be observed in the 2-D WPS at regular intervals. These are likely secondary tones of the vortex shedding that are visible due to the lack of turbulence in the boundary layer.

Table 3. WPS extracted BVS shedding frequencies and peak amplitudes.

Case	r/R	Freq. (kHz)	St	Peak (dB)
2-D Airfoil	0.55	10.184	0.0987	125.91
Rotor	0.55	10.313	0.101	117.38
2-D Airfoil	0.65	12.117	0.0996	131.45
Rotor	0.65	12.117	0.0997	123.51
2-D Airfoil	0.75	13.664	0.0978	135.21
3-D Airfoil	0.75	13.277	0.0951	128.05
Rotor	0.75	13.535	0.0972	128.38

Plotted as power spectra in dB, the peak WPS amplitudes from the 2-D airfoil simulations overpredict the peak amplitudes of the 3-D rotor simulations by 7 to 8 dB but follow the peak

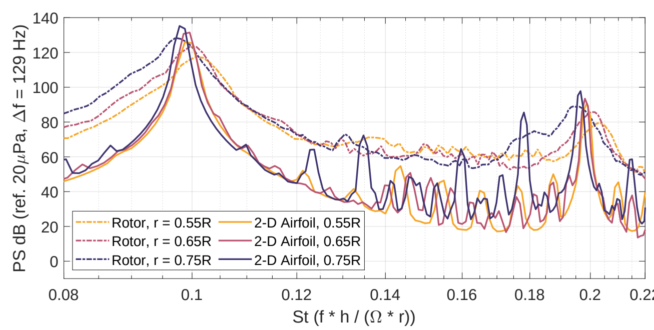

Figure 24. Wall pressure spectra at the suction side TE from r = 0.55R, 0.65R, and 0.75R for both 2D airfoil and rotor simulations, scaled by Strouhal number.

trends well. The overprediction in surface pressure fluctuations is expected from a 2-D simulation that assumes infinite spanwise coherence and has no mechanism for spanwise vortex stretching.

To help confirm that the peak frequency corresponds to BVS shedding, the same data is re-ploted in Figure 24 but with frequency scaled by Strouhal number. In general, the peak shedding frequencies collapse to St = 0.1. However, both the 2-D airfoil and rotor station for r = 0.75R show the BVS peak occurring at a slightly lower Strouhal number than 0.1. As previously mentioned, the presence of the vortex wake field in the rotor simulation might be influencing the freestream velocity and angle of attack at the r = 0.75R blade station, which would carry over to inputs to the 2-D airfoil simulation. Additionally, each simulation is at a different angle of attack, which could influence the shedding frequencies, but this remains a topic for future investigation.

Additionally, for the r = 0.75R station, a spectral hump is observed in both the 2-D and rotor WPS near St = 0.178. This

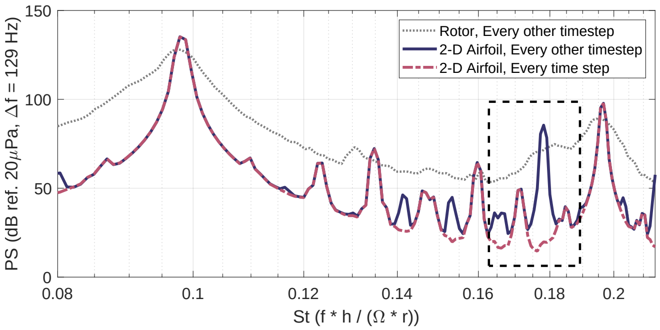

Figure 25. Wall pressure spectra at the suction side TE from r = 0.75R for both 2D airfoil and rotor simulations, scaled by Strouhal number

peak is not the second harmonic, which occurs just below St = 0.2. While at first it seems like the 2-D simulation is capturing some additional flowfield feature or noise source, this small peak is assumed to be caused by aliasing effects. Figure 25 shows the rotor and 2-D airfoil WPS for the r = 0.75R station, processed with wall pressures at every other timestep from the simulation, which is how all results were processed in this work. Wall pressures at every timestep were available from the 2-D airfoil simulation, were processed at the same spectral bin width (132 Hz), and were plotted in Figure 25 for comparison. The peak BVS and secondary harmonic peaks are identical, but other lower-amplitude peaks appear and disappear. Specifically, the small spectral peak around St = 0.178, highlighted by the dashed black box, disappears in the spectra processed at each timestep, which indicates an aliasing effect due to the effective downsampling of the surface pressure data. This is an indication that care should be taken to properly discretize the unsteady fluid nature of the vortex shedding and to sample wall pressures at an appropriate rate since downsampling an already coarse signal could exacerbate aliasing issues. Even with caveats regarding timestep size and discretization, the 2-D airfoil simulations clearly capture the trend behavior of BVS along the ITR blade span.

The computational cost of the 2-D airfoil simulations is greatly reduced compared to running a 3-D rotor simulation. Thurman et al. (Ref. 18) noted that the cost of the rotor simulation per revolution is 700 CPU hours. Converting this cost to an airfoil-related metric, convective time unit (CTU), the cost at the r = 0.55R blade station (due to sectional velocity and rotor period) is 40.32 CPU hours per CTU. In comparison, the cost of the entire 2-D airfoil simulation from startup to writing data at the same r = 0.55R station is 0.42 CPU hours per CTU, which is an approximately 100x decrease in computational time.

3-D Airfoil Simulations

Several 3-D airfoil simulations were also performed to determine if there are any effects on the BVS frequency and amplitude. It is recognized that although BVS is a quasi-2-D phenomena, spanwise vortex stretching could play a role. A single 3-D airfoil simulation is discussed here.

The r = 0.75R airfoil grid was extruded in the spanwise direction with a fixed spacing, using 65 points in a span of $0.3 \cdot c$ (195 points / chord). The flow conditions were the same as listed in Table 2 for the r = 0.75R station and the 2-D simulation flowfield was extruded and used to initialize the 3-D simulation.

With SA-DDES, the spanwise spacing can play a role in the switch from RANS to LES. Several combinations of spanwise distance and number of points were tried, but ultimately it was discovered that BVS could not be predicted with a number of spanwise points that was representative of DDES and not LES.

With coarser spanwise spacings, the 3-D airfoil simulations tended toward a steady RANS recirculation region in the near-wake instead of alternating vortex shedding. The likely cause of this limitation is suspected to be the DDES shielding function, f_d, that governs the switch from RANS to LES in the near-wake (Ref. 24). For this simulation, the number of spanwise points was chosen because BVS shedding was not observed with fewer points in the span.

Figure 26 plots contours of f_d, where 0 indicates RANS (purple) and 1 indicates LES (yellow). Figure 26(a) is taken from the 2-D airfoil simulation at r = 0.75R while Figure 26(b) is taken from the 3-D airfoil simulation. The 2-D airfoil simulation shows a clear LES region downstream of the TE in the near-wake, which is ensured because the spanwise components of the DDES filter are disabled for 2-D simulations. In contrast, a triangular RANS region downstream of the TE can be observed for the 3-D airfoil that extends into the vortex shedding region. Although BVS was predicted in this case, it is likely that this RANS region negatively influenced the vortex roll-up and shedding behavior in this case and outright prevented BVS in other cases with coarser grid spacing.

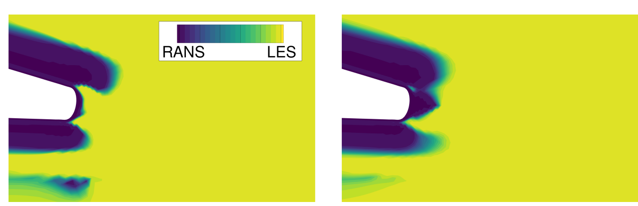

(a) 2-D Airfoil (b) 3-D Airfoil

Figure 26. Contours of f_d, the DDES shielding function.

Even with a large number of spanwise points, the simulation still predicted the 3-D equivalent of 2-D vortex shedding, with a perfectly coherent vortex along the span. Figure 27 shows an isosurface of Q-criterion colored by spanwise vorticity. Although vortices of alternating direction are shed, the lack of spanwise variation is apparent. Indeed, it is likely that for 3-D airfoils without crossflow or turbulence (due to modeling or grid spacing), there may be no instability to break up the spanwise coherence. In limited preliminary tests, when the grid spacing was made fine enough for Tollmein-Schlicting

Table 4. **BVS shedding frequencies and peak farfield amplitudes.**

Case	r/R	h/δ^*_{avg}	Frequency (kHz)	St	Span / chord	Farfield SPL (dB)
2-D Airfoil	0.55	0.912	10.262	0.0995	62.99	89.27
2-D Airfoil (α_{BEMT})	0.55	0.901	10.130	0.0982	62.99	89.00
Rotor	0.55	–	10.394	0.101	0.03780	82.03
2-D Airfoil	0.65	0.928	12.103	0.0995	62.99	98.54
Rotor	0.65	–	12.104	0.0995	0.03465	88.43
2-D Airfoil	0.75	0.938	13.682	0.0980	62.99	100.22
3-D Airfoil	0.75	–	13.288	0.0952	0.3000	100.14
Rotor	0.75	–	13.814	0.0989	0.03118	96.25

waves to develop, only then was the spanwise coherence significantly disrupted.

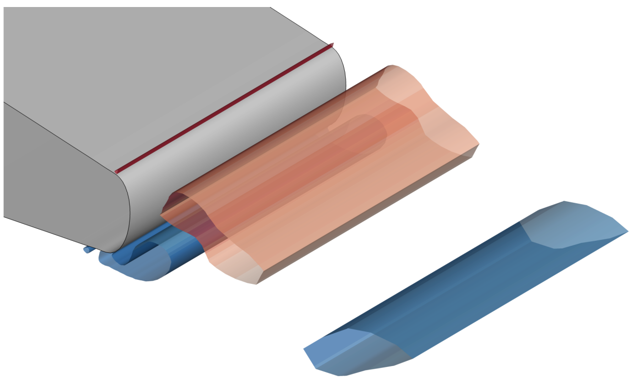

Figure 27. Isosurface of Q-criterion showing coherent BVS along the entire span of a 3-D airfoil simulation. Colored by spanwise vorticity (red = positive rotation, blue = negative rotation).

The WPS from the centerline of the 3-D airfoil simulation at the suction side of the TE was extracted and plotted in Figure 28 to compare to the 2-D airfoil and rotor simulations. The shedding frequency predicted by the 3-D simulation, plotted in Strohual number, is lower than for the 2-D simulation by 387 Hz (see Table 3). A similar result was observed by Stone et al. (Ref. 13) who predicted vortex shedding from 2-D and 3-D airfoils with largely blunt trailing edges. In general, Stone et al. showed a slight decrease in shedding frequency from 2-D to 3-D, and they concluded that the main advantage of a 3-D simulation was an improved drag calculation, which is not a concern here. The 3-D airfoil simulation does not show the widened spectral hump like the rotor spectra, but a narrow peak like the 2-D airfoil simulations. The spectral floor of the WPS is increased overall in the 3-D simulation and small peaks between the fundamental and second harmonic frequencies are not observed like in the 2-D WPS.

The simulated airfoil had a spanwise z+ of around 25, which is nearly LES-level grid spacing. Multiple simulations of this size would be prohibitively expensive and strays from the intent of using DDES to reduce computational expense. For the present simulations, there is no apparent advantage to 3-D DDES. Given the excellent agreement between the 2-D airfoil

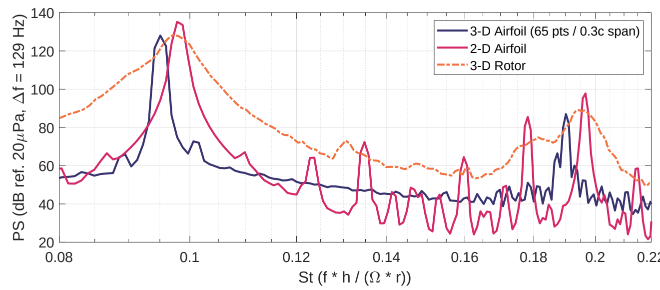

Figure 28. Trailing edge wall pressure fluctuations from 2-D and 3-D airfoils and the r = 0.75R rotor blade station.

and rotor WPS, it was decided that no additional 3-D airfoil simulations would be included in this work.

Farfield BVS Noise Predictions

A last piece of the puzzle for the 2-D airfoil simulations is predicting farfield BVS noise from the wall pressure fluctuations using F1A. Since area is included in the F1A integration for farfield noise, the spanwise extent of the rotor stations and the 2-D airfoils must be adjusted to properly compare the farfield noise. The spanwise width of each simulated section is given in Table 4. For the rotor sections, the spanwise extent is defined by the local grid spacing. The airfoil grids had three spanwise points in order to solve the 2-D problem in OVERFLOW2, which resulted in a grid span of 2 grid units (meters in this case). Once the acoustic pressure time-histories were computed from F1A, the pressures from all simulations were scaled to an equivalent span of 1.0 m (3.28 ft). Although this pressure scaling is valid for the 2-D airfoil simulations, it is not technically correct for the rotor sections since the spanwise variation in pressures are included in the noise integration. However, the spanwise width is small enough that the spanwise variation can be assumed approximately constant.

The observer location was placed in the farfield directly above the trailing edge. To eliminate Doppler shift effects, the rotor grid was fixed in place such that the observer remained a consistent distance from the trailing edge. The observer was placed 1.0 m (3.28 ft) or 31.496 chords above the TE, at 90° to the chord, and at the spanwise centerline of each 2-D airfoil simulation or the mid-span of each rotor blade section.

Using only the loading component from F1A, farfield sound pressure levels (SPL) were computed at the TE-fixed observer.

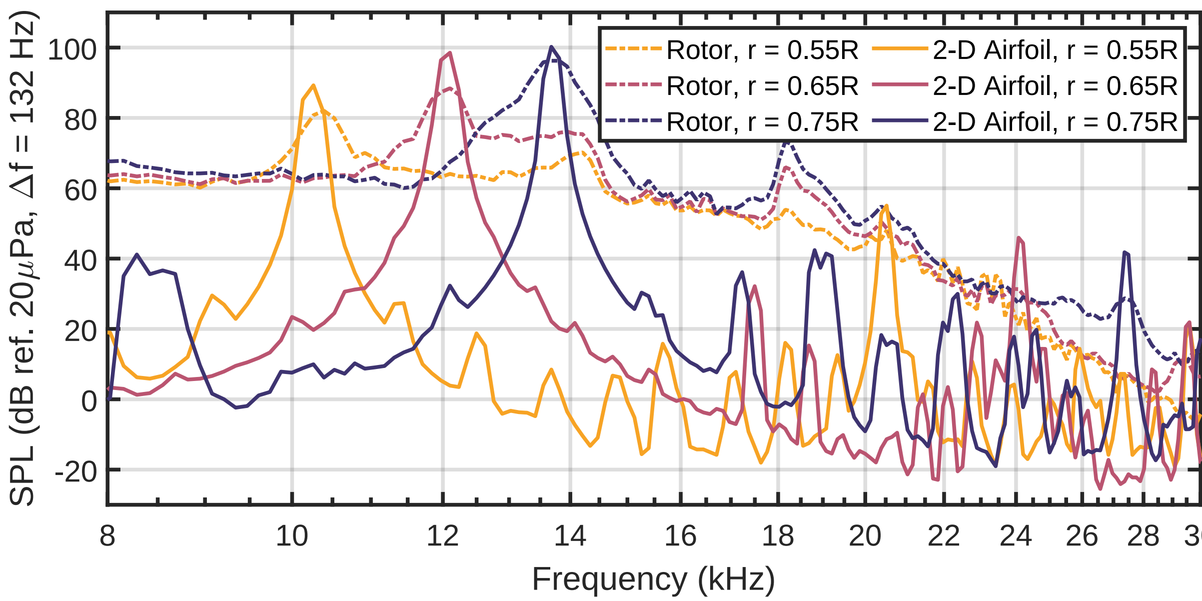

Figure 29. Farfield noise predictions for the three rotor stations and airfoils at 1.0 m (3.28 ft) above each trailing edge.

Figure 29 shows farfield SPL for the three 2-D rotor and airfoil station simulations. The trend is increasing peak amplitude with increasing shedding frequency, and the peak frequencies match well between the 2-D airfoil and rotor simulations. Frequency peaks from other noise sources can be seen in the rotor spectra. The second harmonic frequency predicted by the 2-D airfoil simulations appears at peaks in the rotor spectra, although additional information is needed to confirm the nature of these peaks.

Table 4 lists the peak frequencies and amplitudes. The peak Strouhal number is approximately 0.1. The 2-D simulations overpredicted farfield noise by 5 to 10 dB, but this trend is expected when simulating quasi-2-D aeroacoustic phenomenon with purely 2-D simulations (Ref. 14). The exception is the r = 0.75R section, which is much closer in amplitude to the rotor noise peak.

Due to the differences in bin widths between the spectral processing of the WPS and farfield noise, there are slight differences in BVS peak frequencies of less than 100 Hz. Still, this agreement in shedding frequency between TE WPS and farfield noise confirms that the peak wall pressure fluctuations do generate BVS noise that is radiated at essentially the same frequencies.

An influential self-noise parameter is δ^*, the displacement thickness of the boundary layer at the trailing edge. The near-wake of the 2-D airfoils was surveyed to extract displacement thickness. Wake lines (see Figure 4)) were placed at the same sampling location used by Brooks, Pope, and Marcolini (Ref. 8). The edge of the boundary layer was determined at $0.99 \cdot V_\infty$ and δ^* was computed via integration of the extracted velocity field in the wake normal to the chord. The suction side and pressure side TE displacement thickness were averaged and non-dimensionalized by the trailing edge thickness, h, to show a thickness ratio, h/δ^*_{avg}. These quantities are listed for the 2-D airfoil simulations in Table 4 for future low-fidelity noise predictions. The average displacement thickness decreases with increasing freestream velocity, which causes the thickness ratio to also increase. Therefore, peak farfield BVS amplitude and shedding frequency both increase with thickness ratio.

The farfield noise was predicted for the 3-D airfoil and amplitudes were corrected to a span of 1 meter. The observer was also placed 1 meter above the TE and at the spanwise centerline. The peak amplitude and frequency are listed in Table 4. There is a 387 Hz difference in shedding frequency, which is approximately a 3% difference from the rotor BVS frequency. Because both simulations essentially modeled BVS with an infinite span, once the span of the two simulations were corrected to the same span, the amplitudes were essentially the same. This suggests that there is no benefit to employing a 3-D DDES simulation for BVS unless some disturbance in the flowfield leads to a spanwise variation. Overall, the 2-D airfoil simulations predict the trends of farfield noise well for the three selected rotor stations.

Application of the 2-D Methodology

The setup for the 2-D airfoil simulations in this work relies on having a 3-D rotor simulation from which to extract flow conditions. The simulation includes the effects of induced velocity and crossflow at each blade station, which results in α_{eff}, an effective angle of attack. An alternative approach would be to estimate the effective angle of attack with BEMT or another low-fidelity aerodynamic solver.

To investigate how the 2-D airfoil method could be applied as a predictive method when α_{eff} cannot be computed from a 3-D simulation, a 2-D simulation at the r = 0.55R blade station was performed with the same freestream velocity and Reynolds number but with the designed angle of attack from BEMT,

α_{BEMT}, at the r = 0.55R blade station (see Table 2). The goal of this simulation was to demonstrate any differences in BVS frequency and amplitude due to the 1.035° increase in α_{BEMT} over α_{eff}.

The farfield noise was predicted for the r = 0.55R airfoil at both angles of attack, and the spectra are shown in Figure 30. The peak amplitudes occur at approximately the same dB level, but the shedding frequency decreases slightly due to the increased α_{BEMT} such that the peak is shifted into the next frequency bin. The decrease in the second harmonic frequency (the peak at approximately 20.4 kHz) also confirms the decreases in BVS frequency. The TE δ^*_{avg} increases with the increase in angle of attack, leading to a decrease of the thickness ratio in Table 4.

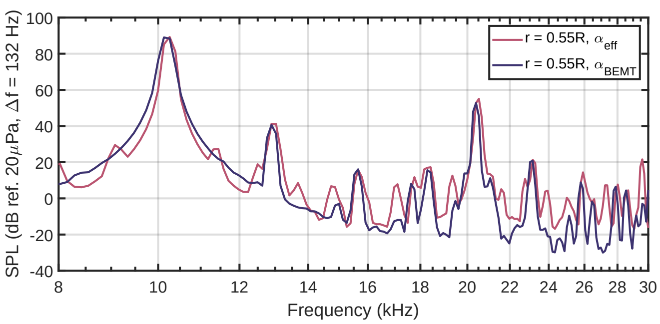

Figure 30. Farfield predictions from 2-D airfoil simulations of r = 0.55R for α_{eff} and α_{BEMT}.

This slight change in shedding frequency and displacement thickness with angle of attack could warrant a future investigation into BVS trends since the effect of angle of attack is not included in the Strouhal scaling. However, the difference in angle of attack between the 3-D simulations and BEMT was small for this case, and the overall effect on the predicted shedding frequency is negligible to the predicted farfield BVS noise. This suggests that, for cases where only BEMT is available to calculate α_{eff}, if the angle is predicted with an accuracy of one or two degrees, the 2-D airfoil method can be applied to estimate BVS noise on a different rotor blade geometry.

CONCLUSIONS

This study demonstrates that 2-D simulations are an appropriate substitution for 3-D rotor simulations when investigating BVS. First, BVS was identified on the rotor through flowfield structures, farfield noise contributions, unsteady loading, and a Strouhal scaling. Region 1 in Figure 8(b) was confirmed to be BVS noise. BVS is not the most significant source on this rotor in terms of peak amplitudes but does appear to contribute to the spectral shape. For the r = 0.55R station, BVS was demonstrated to exist in the simulation through an analysis of near-field flowfield features, fluctuating wall pressures, coherence, phase, and Strouhal scaling. The width of the spectral shape of the BVS peaks from the rotor simulation is assumed to be caused by the spanwise variation of shedding frequency along the blade and by neighboring BVS events being "felt" at the blade stations under investigation.

With confidence that BVS was correctly identified at three blade stations, r = 0.55R, 0.65R, and 0.75R, 2-D airfoil simulations were performed at flow conditions corresponding to the three rotor stations. It should be noted that the chosen rotor stations were relatively free of 3-D flow effects such as BWI and that crossflow and radial flow effects appear to be negligible for the chosen blade stations. Flowfield visualizations and wall pressure analysis again confirmed the existence of BVS. The BVS WPS from the 2-D airfoil simulations demonstrated the same trends in BVS frequency and peak amplitude as the three blade stations from the rotor simulation.

Next, 3-D airfoil simulations were performed but BVS was suppressed by the SA-DDES shielding function when the spanwise gird spacing was not fine enough. This required a prohibitively large number of points in the spanwise direction to predict BVS in the 3-D simulation. Combined with the fact that the predicted BVS frequencies from the 2-D airfoil simulations showed excellent agreement with the rotor station shedding frequencies, the benefit of 3-D SA-DDES airfoil simulations did not appear to be worth the increased computational cost for this application.

Finally, farfield BVS noise was predicted from the 2-D airfoils using F1A. Again, trends of BVS frequency and peak amplitude from the selected rotor stations were replicated and the peak frequencies were predicted within 2%. The amplitude of the farfield noise appears to be overpredicted by 5–10 dB with the 2-D airfoil method as compared to the rotor simulation. The incident wall pressure fluctuations of the 2-D BVS appears slightly stronger than the BVS from the rotor simulation, which is expected because of the infinite spanwise vortex. This extra strength contributes to the overprediction of farfield noise amplitudes. A single 2-D airfoil simulation showed that predicting the BVS shedding frequency with a BEMT-computed α_{eff} led to a negligible change in shedding frequency and amplitude, which suggests that this method could be applied when a full 3-D rotor simulation is not feasible.

These results give confidence that a simplified 2-D hybrid RANS/LES airfoil simulation approach can:

1. isolate BVS for self-noise predictions.
2. replicate spanwise BVS trends in WPS and farfield noise from the 3-D ITR simulation (the shedding frequency was predicted within 2% and the amplitude within 5–10 dB).
3. achieve a significant reduction in computational cost (nearly a 100x decrease compared to the 3-D rotor simulation) without a significant reduction in fidelity.

Although computationally cheap compared to a rotor simulation, the 2-D approach is probably still too expensive to be applied in a rotor design optimization framework. The 2-D approach could, however, be used to predict trends in BVS self-noise with important geometric and flow parameters in order to improve low-fidelity broadband models like BPM (Brooks, Pope, and Marcolini) (Ref. 8). Updated low-fidelity models could then be used for rotor design optimization.

This 2-D approach could also be used to investigate BVS noise from other rotor geometries by simulating a few selected blade stations (r = 0.75R, for example). For instance, low-fidelity predictions of BVS noise for the three-bladed COPR (computationally optimized proprotor) in forward flight (Ref. 4) showed a wide spectral BVS hump due to a spanwise variation of trailing edge thickness along the blade. The present modeling approach could help confirm the predicted spanwise variation in BVS.

Author contact:
Joshua D. Blake, joshua.d.blake@nasa.gov
Christopher S. Thurman, christopher.thurman@nasa.gov
Nikolas S. Zawodny, nikolas.s.zawodny@nasa.gov

ACKNOWLEDGMENTS

The authors would like to thank Len Lopes for help with ANOPP2 metadata and Doug Boyd with OVERFLOW2 wake sampling, both from the Aeroacoustics Branch at NASA Langley. Computational resources supporting this work were provided by the Midrange HPC K-Cluster located at NASA's Langley Research Center. This work was funded by the NASA Revolutionary Vertical Lift Technology (RVLT) project.

REFERENCES

1. Greenwood, E., Brentner, K. S., Rau, R. F., and Ted Gan, Z. F., "Challenges and Opportunities for Low Noise Electric Aircraft," *International Journal of Aeroacoustics*, Vol. 21, (5–7), 2022, pp. 315–381. DOI: 10.1177/1475472X221107377.

2. Zawodny, N. S., Boyd, D. D., and Burley, C., "Acoustic Characterization and Prediction of Representative, Small-Scale Rotary-Wing Unmanned Aircraft System Components," AHS International 72nd Annual Forum & Technology Display, West Palm Beach, Florida, May 2016. DOI: 10.4050/F-0072-2016-11346.

3. Pettingill, N. A., Zawodny, N. S., Thurman, C., and Lopes, L. V., "Acoustic and Performance Characteristics of an Ideally Twisted Rotor in Hover," AIAA Paper 2021–1928, AIAA SciTech 2021 Forum, January 2021. DOI: 10.2514/6.2021-1928.

4. Blake, J. D., Thurman, C. S., Zawodny, N. S., and Lopes, L. V., "Broadband Predictions of Optimized Proprotors in Axial Forward Flight," AIAA Paper 2023–4183, AIAA AVIATION 2023 Forum, June 2023. DOI: 10.2514/6.2023-4183.

5. Thurman, C., Zawodny, N. S., Pettingill, N. A., Lopes, L. V., and Baeder, J. D., "Physics-informed Broadband Noise Source Identification and Prediction of an Ideally Twisted Rotor," AIAA Paper 2021–1925, AIAA SciTech 2021 Forum, January 2021. DOI: 10.2514/6.2021-1925.

6. Thurman, C., Boyd, D. D., and Lopes, L. V., "Prediction of Broadband Blade-Wake Back-Scatter Noise from a Hovering Ideally Twisted Rotor using OVERFLOW2-ANOPP2," AIAA Paper 2024–2471, AIAA SciTech 2024 Forum, January 8–12, 2024. DOI: 10.2514/6.2024-2471.

7. Brooks, T., and Hodgson, T., "Trailing Edge Noise Prediction from Measured Surface Pressures," *Journal of Sound and Vibration*, Vol. 78, (1), 1981, pp. 69–117. DOI: 10.1016/S0022-460X(81)80158-7.

8. Brooks, T. F., Pope, D. S., and Marcolini, M. A., "Airfoil Self-Noise and Prediction," NASA RP 1218, National Aeronautics and Space Administration, July 1989.

9. Tam, C. K. W., and Ju, H., "Aerofoil Tones at Moderate Reynolds Number," *Journal of Fluid Mechanics*, Vol. 690, 2012, pp. 536–570. DOI: 10.1017/jfm.2011.465.

10. Paterson, R. W., Vogt, P. G., Fink, M. R., and Munch, C. L., "Vortex Noise of Isolated Airfoils," *Journal of Aircraft*, Vol. 10, (5), 1973, pp. 296–302. DOI: 10.2514/3.60229.

11. Roger, M., and Moreau, S., "Extensions and Limitations of Analytical Airfoil Broadband Noise Models," *International Journal of Aeroacoustics*, Vol. 9, (3), 2010, pp. 273–305. DOI: 10.1260/1475-472X.9.3.273.

12. Metzinger, C. N., Chow, R., Baker, J. P., Cooperman, A. M., and van Dam, C. P., "Experimental and Computational Investigation of Blunt Trailing-Edge Airfoils with Splitter Plates," *AIAA Journal*, Vol. 56, (8), 2018, pp. 3229–3239. DOI: 10.2514/1.J056098.

13. Stone, C., Barone, M., Smith, M., and Lynch, E., "A Computational Study of the Aerodynamics and Aeroacoustics of a Flatback Airfoil Using Hybrid RANS-LES," AIAA Paper 2009–273, 47th AIAA Aerospace Sciences Meeting including The New Horizons Forum and Aerospace Exposition, January 2009. DOI: 10.2514/6.2009-273.

14. Singer, B. A., Lockard, D. P., and Brentner, K. S., "Computational Aeroacoustic Analysis of Slat Trailing-Edge Flow," *AIAA Journal*, Vol. 38, (9), 2000, pp. 1558–1564. DOI: 10.2514/2.1177.

15. Le Garrec, T., Gloerfelt, X., and Corre, C., "Direct Noise Computation of Trailing Edge Noise at High Reynolds Numbers," AIAA Paper 2008–2914, 14th AIAA/CEAS Aeroacoustics Conference (29th AIAA Aeroacoustics Conference), May 2008. DOI: 10.2514/6.2008-2914.

16. Wolf, W. R., Azevedo, J. L. F., and Lele, S. K., "Convective Effects and the Role of Quadrupole Sources for Aerofoil Aeroacoustics," *Journal of Fluid Mechanics*, Vol. 708, 2012, pp. 502–538. DOI: 10.1017/jfm.2012.327.

17. Xing, Y., Chen, W., Wang, X., Tong, F., and Qiao, W., "Effect of Wavy Leading Edges on Airfoil Trailing-Edge Bluntness Noise," *Aerospace*, Vol. 10, (4), 2023. DOI: 10.3390/aerospace10040353.

18. Thurman, C., Boyd Jr., D. D., Buning, P., Reboul, G., and Benoit, C., "NASA/ONERA Collaboration on Small Hovering Rotor Broadband Noise Prediction Using Lattice-Boltzmann Method and Structured Navier-Stokes Solvers," AIAA Paper 2024–3106, 30th AIAA/CEAS Aeroacoustics Conference, June 4–7, 2024. DOI: 10.2514/6.2024-3106.

19. McDonald, R. A., and Gloudemans, J. R., "Open Vehicle Sketch Pad: An Open Source Parametric Geometry and Analysis Tool for Conceptual Aircraft Design," AIAA Paper 2022–0004, AIAA SciTech 2022 Forum, 2022. DOI: 10.2514/6.2022-0004.

20. Nichols, R. H., Tramel, R. W., and Buning, P. G., "Solver and Turbulence Model Upgrades to OVERFLOW 2 for Unsteady and High-Speed Applications," 24th Applied Aerodynamics Conference, June 2006. DOI: 10.2514/6.2006-2824.

21. Benek, J. A., Buning, P. G., and Steger, J. L., "A 3-D CHIMERA Grid Embedding Technique," AIAA Paper 85–1523, 7th Computational Physics Conference, July 1985. DOI: 10.2514/6.1985-1523.

22. Tramel, R. W., Nichols, R. H., and Buning, P. G., "Addition of Improved Shock-Capturing Schemes to OVERFLOW 2.1," AIAA Paper 2009–3988, 19th AIAA Computational Fluid Dynamics Conference, June 2009. DOI: 10.2514/6.2009-3988.

23. Derlaga, J. M., Jackson, C. W., and Buning, P. G., "Recent Progress in OVERFLOW Convergence Improvements," AIAA Paper 2020–1045, AIAA SciTech 2020 Forum, January 6–10, 2020. DOI: 10.2514/6.2020-1045.

24. Spalart, P. R., Deck, S., Shur, M. L., Squires, K. D., Strelets, M. K., and Travin, A., "A New Version of Detached-eddy Simulation, Resistant to Ambiguous Grid Densities," *Theoretical and Computational Fluid Dynamics*, Vol. 20, 2006, pp. 181–195. DOI: 10.1007/s00162-006-0015-0.

25. Chan, W. M., Gomez, R. J., Rogers, S. E., and Buning, P. G., "Best Practices in Overset Grid Generation," AIAA Paper 2002–3191, 32nd AIAA Fluid Dynamics Conference and Exhibit, June 2002. DOI: 10.2514/6.2002-3191.

26. Lopes, L., "ANOPP2's Farassat Formulations Internal Functional Modules (AFFIFMs) Reference Manual," NASA TM 2021-0021111, 2021.